Polarizable dipole models for reflectance anisotropy spectroscopy: a review

2004 J. Phys.: Condens. Matter 16 S4259

(http://iopscience.iop.org/0953-8984/16/39/002)

INSTITUTE OF PHYSICS PUBLISHING JOURNAL OF PHYSICS: CONDENSED MATTER

J. Phys.: Condens. Matter **16** (2004) S4259–S4278 PII: S0953-8984(04)79689-7

Polarizable dipole models for reflectance anisotropy spectroscopy: a review

N Arzate, B S Mendoza[1] and R A Vázquez-Nava

Centro de Investigaciones en Optica AC, León Guanajuato, Mexico

E-mail: bms@cio.mx

Received 21 April 2004
Published 17 September 2004
Online at stacks.iop.org/JPhysCM/16/S4259
doi:10.1088/0953-8984/16/39/002

Abstract

We present a review of the formalism and application of polarizable dipole models that have been used to calculate reflectance anisotropy spectra of semiconductor and metal surfaces and thin organic films.

1. Introduction

Optical spectroscopic techniques are increasingly used nowadays to investigate surfaces and interfaces. This is because of their high time resolution, the fact that they present in general only small perturbations to the system studied and that they deliver new information about the electronic states (chemical information). Both linear and non-linear optical probes are employed to investigate very different physical aspects of surfaces with great success [1–4]. In particular reflectance anisotropy spectroscopy (RAS) has received a lot of attention both experimentally and theoretically, since it is one of the few optical techniques that probes directly the surface and interface structure of cubic materials. RAS measures the difference between the normal-incidence optical reflectance of light polarized along the two principal axes in the surface plane as a function of the photon energy. Since the bulk optical properties of cubic crystals are isotropic, any observed anisotropy must be related to the lower symmetry of the surface. RAS data are typically obtained in the visible–ultraviolet spectral range, thus providing information about electronic structure modifications due to the creation of the surface, reconstructions, adsorbates, etc [5–7]. On one hand, the experiments are rather simple to perform and a high degree of sophistication in data acquisition is now possible [8, 9]. On the other hand, the comparison of experimental and calculated RAS has served as a benchmark of various degrees of refinement in the theoretical description of the phenomena. For semiconductor systems, these calculations range from the phenomenological polarizable dipole models (see references below), where it is worth mentioning the pioneering work of [10],

[1] Author to whom any correspondence should be addressed.

semi-empirical models [11–13], *ab initio* models [14, 15], through the more sophisticated ones where excitonic effects are taken into account [16, 17].

In this paper, we review only the polarizable dipole models (PDMs) that have been used to calculate RAS spectra. These models have the advantage of a simple interpretation, and although not fully microscopic, they capture some of the basic physics involved in the interaction of light and the surface of the system in question. In the discrete dipole model the optical response of a medium is approximated by the response of an ordered array of suitable polarizable units to an applied electric field. Such polarizable units are coupled together by the electric field produced by dipole moments induced in the polarizable neighbouring sites, i.e. the local field. Polarizable dipole descriptions for both bulk and surface systems of crystals have been treated in the literature [18–42] to calculate linear [28, 41, 43–49] and nonlinear [43, 44, 46, 50–57] optical properties of metal and semiconductor surfaces; they have been used to calculate linear [58, 59] and nonlinear [59–62] optical properties of thin organic films and fractal aggregates [63] as well. In particular, at crystalline surfaces the discrete dipole model has been used to calculate the RAS spectra of Ge(110) [49], GaAs(110) [64] and of several Si surfaces [43–46, 65, 66].

As we will see in this review, the calculation of the PDM, encompasses two major steps. The first one is the calculation of the microscopic linear polarizability of the polarizable unit, and the second step is related to the calculation of the local field, for which the interaction of all the units in the system must be taken into account. The models that are described below basically differ in the first step, since, regardless of the origin of the microscopic polarizability, the calculation of the local field is achieved by the standard method of the *plane wise summation* [67]. Thus, we classify the works according to the following scheme. Phenomenological models in which the polarizability is calculated with the help of the experimental bulk dielectric function through the use of the Clausius–Mossotti relation. Local models, where a *dressed* polarizability is calculated through *ab initio* methods based on the generalized valence bond scheme and, the non-local models that take into account the non-locality in the electro-dynamical and quantum-mechanical interactions through the use of both real space local fields and *ab initio* non-local polarizabilities.

The article is organized as follows. In section 2 we present the basic equations for the PDM. Then in sections 3–5, we discuss and present results of the non-local, local and phenomenological models, respectively. Finally in section 6 we give the conclusions and outlook of the PDM.

2. General formalism

We start with a general model that one can use to calculate the induced polarization of a given system. Then, through this polarization we show how the RAS signal can be obtained. The constitutive equation relating the induced polarization density at point $\boldsymbol{r}$, $\boldsymbol{P}$ to the self-consistent perturbing electric field of frequency ω, $\boldsymbol{E}$, is given by

$$\boldsymbol{P}(\boldsymbol{r},\omega) = \int \boldsymbol{\chi}(\boldsymbol{r},\boldsymbol{r}',\omega)\cdot\boldsymbol{E}(\boldsymbol{r}',\omega)\,\mathrm{d}\boldsymbol{r}', \tag{1}$$

where $\boldsymbol{\chi}(\boldsymbol{r},\boldsymbol{r}',\omega)$ is the non-local linear susceptibility tensor. To calculate the self-consistent field, we add to the external field $\boldsymbol{E}^{\mathrm{ext}}$, the field induced by the polarization, then

$$\boldsymbol{E}(\boldsymbol{r},\omega) = \boldsymbol{E}^{\mathrm{ext}}(\boldsymbol{r},\omega) + \int \boldsymbol{f}(\boldsymbol{r}-\boldsymbol{r}',\omega)\cdot\boldsymbol{P}(\boldsymbol{r}',\omega)\,\mathrm{d}\boldsymbol{r}' \tag{2}$$

where the transfer kernel $\boldsymbol{f}(\boldsymbol{r}-\boldsymbol{r}',\omega)$ describes the full non-local retarded electro-magnetic interaction and is given by

$$f_{\mu\nu}(\boldsymbol{r},\omega)=(k^2\delta_{\mu\nu}+\nabla_\mu\nabla_\nu)\frac{\exp(\mathrm{i}kr)}{r}, \tag{3}$$

with μ, ν the Cartesian components, $k=\omega/c$ is the wavenumber with c the speed light, and $r=|\boldsymbol{r}|$. In general, the direct solution of the microscopic equations (1) and (2) is not tractable for large systems such as realistic surfaces. Then, we should make some simplifications in order to have a tractable model.

First, we divide the system in question into a collection of cells, each cell containing one polarizable unit. The interactions between the cells are given by equation (3) and inside the cells an appropriate averaging scheme is used. This approach makes the calculation feasible. The electromagnetic response of an individual cell is considered to be a point-like dipole which represents the polarization of a single cell i with volume V_i. The position of the dipole denoted by $\boldsymbol{r}_i$ could be located at the centre of the cell or at any other position within the cell according to the physical situation at hand. The dipole strength of the ith cell is then a simple average over its volume,

$$\boldsymbol{P}_i(\omega)=\int_{V_i}\boldsymbol{P}(\boldsymbol{r},\omega)\,\mathrm{d}\boldsymbol{r}. \tag{4}$$

Within the same idea we can average the non-local susceptibility tensor in order to define the non-local polarizability tensor, $\boldsymbol{\alpha}_{ij}(\omega)$, through

$$\boldsymbol{\alpha}_{ij}(\omega)=\int_{V_i}\mathrm{d}\boldsymbol{r}\int_{V_j}\mathrm{d}\boldsymbol{r}'\,\boldsymbol{\chi}(\boldsymbol{r},\boldsymbol{r}',\omega), \tag{5}$$

that relates the linear response of cell i and j. Then we assume a uniform external field $\boldsymbol{E}^{\mathrm{ext}}(\omega)$ within each cell, and note that since $\boldsymbol{f}_{ij}$ is evaluated at $r=|\boldsymbol{r}_i-\boldsymbol{r}_j|$ with $\boldsymbol{r}_i$ and $\boldsymbol{r}_j$ the fixed positions of the corresponding dipoles, it can be taken as constant and thus out of any integration symbol. Therefore, after substituting equation (2) into (1), we can easily average $\boldsymbol{P}(\boldsymbol{r},\omega)$ to obtain

$$\boldsymbol{P}_i(\omega)=\sum_j\boldsymbol{\alpha}_{ij}(\omega)\left[\boldsymbol{E}_j^{\mathrm{ext}}+\sum_k\boldsymbol{f}_{jk}(\omega)\cdot\boldsymbol{P}_k(\omega)\right], \tag{6}$$

where the term in brackets is the local field, which is recognized as the external field plus the dipolar field produced by all the dipoles. Equation (6) is a set of equations that have to be solved self-consistently for all the induced dipole moments $\boldsymbol{P}_i$ of the system and defines the essence of the PDM.

In general, to study RAS we have to deal with a surface or overlayer which sits on top of an isotropic bulk, and in order to use the PDM one has to solve equation (6) for a semi-infinite or finite system of polarizable units. This is done by a plane wise technique, by which the system is decomposed in suitable planes perpendicular to the normal direction of the surface, and the dipole moment acquired by each polarizable unit in a given plane is the same for all the units in this plane. Then one typically has to calculate $\boldsymbol{P}_n(\omega)$ as a function of the plane index n, starting at $n=0$ (i.e. the surface), and proceeding towards the bulk, i.e. $n=\infty$, which should give the bulk polarization $\boldsymbol{P}_{\mathrm{B}}(\omega)$.

Once this is done, one can follow the model of [68] or [49] in order to get the reflectivity of the system, since both give essentially the same result. Defining the RAS signal as

$$\mathrm{RAS}\equiv\frac{\Delta R_x-\Delta R_y}{R}, \tag{7}$$

where ΔR_i is the surface related change in the reflectivity and R is the usual Fresnel reflectivity, where we have taken the normally-incident light to be polarized along $i = x$ or y (both x and y are in the surface plane). Then we see that the RAS signal is defined as the normalized change in reflectivity along two mutually perpendicular surface directions. From [49] we get that

$$\mathrm{RAS} = \frac{4d\omega}{c}\,\mathrm{Re}\left[\mathrm{i}(1-\epsilon(\omega))\sum_{n\geqslant 0}\frac{P_n^x(\omega)-P_n^y(\omega)}{P_{\mathrm{B}}(\omega)}\right], \tag{8}$$

where d is the plane separation, $\epsilon(\omega)$ is the bulk dielectric function, $P_n^i(\omega)$ is the induced dipole moment of plane n along the ith direction and $P_{\mathrm{B}}(\omega)$ is the bulk dipole moment, which is isotropic. Note that the summation in equation (8) is well defined since as $n \to \infty$, P_n^i goes to the bulk value and becomes isotropic.

With the help of equations (6) and (8), and subsequent definitions, we have a closed set of equations through which we can calculate the RAS spectra, once the microscopic information of the response of the polarizable units, given by $\boldsymbol{\alpha}_{ij}$, is provided. As we mention before, the computation of $\boldsymbol{f}_{jk}$ is the same, regardless of the model used to calculate $\boldsymbol{\alpha}_{ij}$. From equation (6) it follows that the basic mechanism driving the optical anisotropy of the surface, within the PDM, is the local field.

A relevant point in the PDM is related to the well known Clausius–Mossotti relation. We recall that

$$\boldsymbol{P}_{\mathrm{B}}(\omega) = \frac{\epsilon(\omega)-1}{4\pi}\boldsymbol{E}_{\mathrm{B}}(\omega), \tag{9}$$

where we introduce the bulk dielectric function $\epsilon(\omega)$, and $\boldsymbol{E}_{\mathrm{B}}(\omega)$ is the electric field in the bulk. This relationship could be used either as a check of consistency or, more importantly, with the help of equation (6), it can be cast in a form that relates the macroscopic $\epsilon(\omega)$ with the microscopic polarizability $\boldsymbol{\alpha}_{ij}$. We call this relationship a generalized Clausius–Mossotti relation, which for a simple cubic crystal and in the long wavelength approximation is given by

$$\frac{\epsilon(\omega)-1}{\epsilon(\omega)+2} = \frac{4\pi}{3}n_0\alpha_{\mathrm{eff}}(\omega), \tag{10}$$

where n_0 is the volume density of polarizable entities (dipoles), and α_{eff} is an effective non-local polarizability [49], that for point polarizable atoms would be the atomic polarizability $\alpha(\omega)$. Note that from the knowledge of $\epsilon(\omega)$ one can obtain $\alpha_{\mathrm{eff}}(\omega)$, either from the simple expression of equation (10) or from the implicit relationship implied by equation (9).

A final remark concerning the local field has to do with the different definitions found for it in the literature. The PDM is given through equation (6), but according to [69] and [70], the local field is incorporated through a Fourier-space analysis of the system's response, where the dielectric function is given by

$$1/\epsilon = [(\boldsymbol{I}+\boldsymbol{T})^{-1}]_{00}, \tag{11}$$

where $\boldsymbol{T}$ is related to the polarizability of the system [70]. Both $\boldsymbol{I}$ (identity) and $\boldsymbol{T}$ are matrices in $\boldsymbol{K}$-space, where $\boldsymbol{K}$ are reciprocal lattice vectors, thus equation (11) requires an inversion of $\boldsymbol{I}+\boldsymbol{T}$ in $\boldsymbol{K}$-space, which zero-zero element gives the reciprocal of the dielectric function. Within this approach, local field effects are introduced as being related to the contribution of all $\boldsymbol{K} \neq 0$ terms. Then, if $\boldsymbol{K} \neq 0$, ϵ of equation (11) contains local field effects, but if $\boldsymbol{K} = 0$, then the dielectric function is simply given through the zero-zero element of $\boldsymbol{T}$, i.e. $\epsilon = 1 + T_{00}$ [70], and no local field effects are included. This means that the spatial dependence of the electron density induced by the atomic structure of the crystal is neglected [71]. As far as we know, it is not clear at all if both definitions are equivalent or to what extent they contain the same physics.

On one hand, microscopic formulations seem to indicate that the $\boldsymbol{K} \neq 0$ contributions to the surface optical response are minimal [16, 72]; on the other hand, the PDM local field is readily responsible for the surface optical anisotropy of the examples presented in this paper. The bridging of these two different definitions of the local field is still an important open question whose answer will benefit surface optics [73], however this topic is beyond the scope of the article.

3. Non-local model

In this section we briefly describe the basic ingredients of the non-local models. From [64], the non-local linear susceptibility is given by

$$\chi(\boldsymbol{r}, \boldsymbol{r}', \omega) = \frac{2}{\omega^2} \sum_{mm'} \frac{\boldsymbol{j}_{mm'}(\boldsymbol{r}) \boldsymbol{j}_{m'm}(\boldsymbol{r}')}{\varepsilon_{m'} - \varepsilon_m - \hbar\omega}, \tag{12}$$

where $\boldsymbol{j}_{mm'}(\boldsymbol{r})$ is the velocity matrix operator, given by

$$\boldsymbol{j}_{mm'}(\boldsymbol{r}) = \frac{\mathrm{i}e\hbar}{2m} \left(\psi_m^*(\boldsymbol{r}) \nabla \psi_{m'}(\boldsymbol{r}) - \psi_{m'}(\boldsymbol{r}) \nabla \psi_m^*(\boldsymbol{r}) \right). \tag{13}$$

The wavefunctions $\psi_m(\boldsymbol{r})$ and energy eigenvalues ε_m are obtained through density functional theory within the local density approximation (DFT-LDA) and using the scissors operator to correct for the underestimation of the band gap. From equation (5) one can get

$$\boldsymbol{\alpha}_{ij}(\omega) = \frac{2}{\omega^2} \sum_{mm'} \frac{\int_{V_i} \mathrm{d}\boldsymbol{r}\, \boldsymbol{j}_{mm'}(\boldsymbol{r}) \int_{V_j} \mathrm{d}\boldsymbol{r}\, \boldsymbol{j}_{m'm}(\boldsymbol{r})}{\varepsilon_{m'} - \varepsilon_m - \hbar\omega}, \tag{14}$$

which is intrinsically non-local. The presence of a perturbing field in one cell causes neighbouring cells to become polarized simultaneously. In general the continuity and differentiability of the wavefunctions is at the basis of this non-local response and extends well beyond the inter-atomic spacing. Whenever the atomic wavefunctions do not overlap considerably, this range will be small and the polarizability is effectively local. However, the non-local models do consider the spilling of the wavefunction outside the cells, and therefore the full non-locality of $\boldsymbol{\alpha}_{ij}$ is taken into account.

The transfer tensors $\boldsymbol{f}_{ij}(\omega)$ can be derived from equation (3) by taking the appropriate cell averages [64]. The intercellular $\boldsymbol{f}_{ij}$ ($i \neq j$) are determined by the transfer kernel between the cell positions $\boldsymbol{r}_i$ and $\boldsymbol{r}_j$. For the intracellular transfer tensor $\boldsymbol{f}_{ii}$ there is a singularity in the transfer kernel. In [64], this problem is overcome by using the approximation of a uniform polarization density, for which the Clausius–Mossotti relation holds (equation (10)), and by comparing experimental and theoretical bulk data through this relationship. The technical details are left for the reader.

To incorporate the non-locality of $\boldsymbol{\alpha}_{ij}$ in the solution of equation (6) for a semi-infinite crystalline system and for a given incident field of the form $\boldsymbol{E}_0 \exp(\mathrm{i}\boldsymbol{k} \cdot \boldsymbol{r})$, the double-cell method is used [41, 40, 64, 74]. Also, a normal mode expansion of the polarization is used and the surface and bulk normal modes are computed through a secular equation derived from equation (6). The solution determines the strengths of the surface and bulk dipoles, through which the RAS signal can be calculated.

By using the previously outlined non-local method, the RAS spectrum for GaAs(110) was calculated in [64]. The theoretical results are shown in figure 1, where bulk values of $\boldsymbol{\alpha}_{ij}$ were used throughout the slab, except for the top-layer atoms. Curve A shows the theoretical non-local RAS for the reconstructed surface, whereas curve B equals curve A but with the RAS of a GaAs bulk terminated system subtracted. Although both curves are in close agreement with

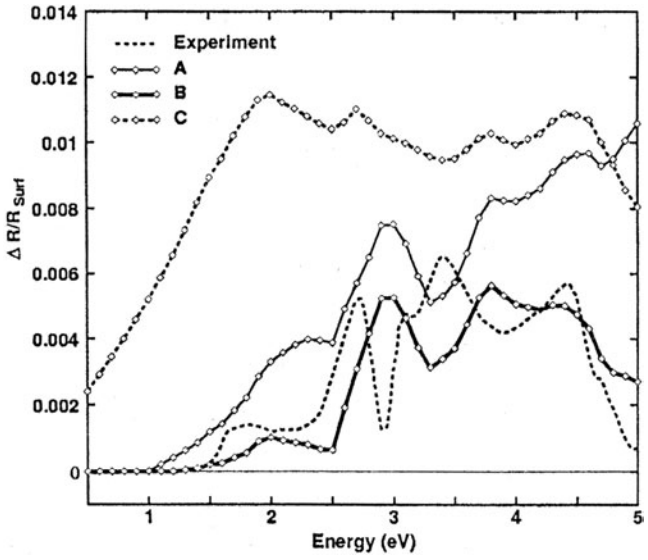

Figure 1. RAS spectra of a GaAs(110) reconstructed surface for the non-local model from [64]. Experimental data from [75]. Curve A is the non-local spectrum, curve B is like curve A but with a bulk terminated system subtracted, and curve C is like B, but with a local polarizability (see text for details). Figure taken from [64].

the experimental observations, the agreement is best for the curve B. The difference between A and B is mainly due to the anisotropy of the bulk. All calculated spectra have the right sign and order of magnitude. Also the spectra structure is remarkably well reproduced apart from a rigid energy shift of 0.3 eV. In curve C the non-local polarizability is made effectively local according to $\boldsymbol{\alpha}_{ij}(\omega) = \delta_{ij} \sum_k \boldsymbol{\alpha}_{ik}(\omega)$. This result shows that surface optical anisotropy depends on the non-local character of the polarizabilities. In [64] it is shown that the non-local character of the polarizabilities hardly influences the average bulk optical properties, like the bulk dielectric function $\epsilon(\omega)$, opposite to the behaviour of the surface optical properties. Therefore the RAS signal is intimately related to the surface atoms, however one has to be aware that within a non-local calculation, no clear distinction can be made between bulk and surface.

4. Local model

In this section we discuss the theoretical framework and present some results of the local model. Two main assumptions are made. One deals with the long wavelength approximation for the incident light, by which the dipoles are considered to be point-like and located at the midpoints of the lines joining neighbouring pairs of atoms, i.e. in the middle of the regions where covalent bonds are located. The other deals with the fact that the polarizability is local. Then, from equation (6), one obtains

$$\boldsymbol{P}_i(\omega) = \boldsymbol{\alpha}_i(\omega)\boldsymbol{E}_i^{\mathrm{loc}} = \boldsymbol{\alpha}_i(\omega)\left[\boldsymbol{E}_i^{\mathrm{ext}}(\omega) + \sum_j \boldsymbol{T}_{ij} \cdot \boldsymbol{P}_j(\omega)\right], \tag{15}$$

where $\boldsymbol{P}_i(\omega)$ is the frequency-dependent dipole moment at site i, $\boldsymbol{\alpha}_i(\omega)$ is a frequency-dependent 3×3 bare polarizability matrix, $\boldsymbol{E}_i^{\mathrm{loc}}$ and $\boldsymbol{E}_i^{\mathrm{ext}}$ are the local and applied fields,

and $\boldsymbol{T}_{ij}$ is a 3×3 transfer matrix that determines the contribution to the local field at site i due to a dipole moment at site j. From equation (3), taking $k = 0$, $\boldsymbol{T}_{ij}$ is given by

$$\boldsymbol{T}_{ij} = \boldsymbol{\nabla}\boldsymbol{\nabla}\frac{1}{|\boldsymbol{r} - \boldsymbol{r}_j|}_{\boldsymbol{r}=\boldsymbol{r}_i}. \tag{16}$$

To obtain the frequency dependent induced dipole moment of equation (15) we assume that for every site i, the tensor $\boldsymbol{\alpha}_i(\omega)$ is diagonal

$$\boldsymbol{\alpha}_i(\omega) = \begin{pmatrix} \alpha^i_{\parallel}(\omega) & 0 & 0 \\ 0 & \alpha^i_{\perp}(\omega) & 0 \\ 0 & 0 & \alpha^i_{\perp'}(\omega) \end{pmatrix}, \tag{17}$$

and represented by a single pole as

$$\alpha^i_{\nu} = \frac{2e^2}{m(\omega^2_{i,\nu} - \omega^2)}, \tag{18}$$

with $\nu = \parallel, \perp, \perp'$ denoting the direction parallel or perpendicular (two-directions) to the dipole axis, respectively. Here, m and e are the mass and the charge of the entity responding to the local field. In the static limit, $\alpha^i_{\nu}(0)$ are calculated through *ab initio* methods and corrected for nearest-neighbour interactions [65].

The homogeneous part of equation (15) (i.e. setting $\boldsymbol{E}^{\mathrm{loc}}_i = 0$), is solved in a slab geometry by assuming Bloch waves for polarization of the form $\boldsymbol{P}_i(\boldsymbol{r}_i) = \boldsymbol{P}_i(\boldsymbol{k}) \exp[\mathrm{i}\boldsymbol{k} \cdot (\boldsymbol{r}_i + \boldsymbol{R})]$, with $\boldsymbol{R}$ the lattice translation vector and $\boldsymbol{k}$ the wavevector of the incident light. The solutions, $\boldsymbol{P}_i(\boldsymbol{k})$, are called *dipole waves*, that from equation (15) obey [66]

$$\left(\boldsymbol{\alpha}^{-1}_i(0)\delta_{ij} - \boldsymbol{T}_{ij}(\boldsymbol{k}) - \lambda^2_n \boldsymbol{I}\delta_{ij}\right) \cdot \boldsymbol{P}_j(\boldsymbol{k}) = 0, \tag{19}$$

where $\boldsymbol{I}$ is a unitary tensor, and in the long wavelength $\boldsymbol{T}_{ij}(\boldsymbol{k}) = \boldsymbol{T}_{ij}(0) = \boldsymbol{T}_{ij}$ of equation (16). Also, the eigenfrequency of the nth dipole wave, Ω_n, is related to the nth eigenvalue of equation (19) by $\lambda^2_n = m\Omega^2_n/2e^2$. For a total of N dipole sites in the system, there are $3N$ eigenvalues n.

Using $\boldsymbol{P}(\boldsymbol{k}, \omega) = \boldsymbol{\alpha}(\boldsymbol{k}, \omega) \cdot \boldsymbol{E}^{\mathrm{ext}}$ as the definition of the so-called dressed bond polarizability of the slab, $\boldsymbol{\alpha}(\boldsymbol{k}, \omega)$, in [66] it is shown that

$$\boldsymbol{\alpha}(\boldsymbol{k}, \omega) = \sum_n \frac{\boldsymbol{P}_n(\boldsymbol{k}_{\parallel})^* \exp[\mathrm{i}k_{\perp}z]\boldsymbol{P}_n(k_{\parallel})}{2m(\Omega^2_n(\boldsymbol{k}_{\parallel}) - \omega^2 - \mathrm{i}\gamma\omega)}, \tag{20}$$

with γ a phenomenological damping parameter, introduced into the denominator to account for absorption of radiation by the slab, and $\boldsymbol{k} = \boldsymbol{k}_{\parallel} + k_{\perp}$. Notice that $\boldsymbol{\alpha}_i(\omega)$ is a bare *site* polarizability, whereas $\boldsymbol{\alpha}(\boldsymbol{k}, \omega)$ is a dressed polarizability that includes interactions with all the dipoles (or bonds) of the system. Through the dressed polarizability, the wavevector and frequency dependent surface and bulk susceptibility tensors are defined through

$$\boldsymbol{\chi}_{\mathrm{s}}(\boldsymbol{k}, \omega) = \frac{1}{V_{\mathrm{s}}} \sum_i^{N_{\mathrm{s}}} \boldsymbol{\alpha}^{\mathrm{s}}_i(\boldsymbol{k}, \omega), \tag{21}$$

with N_{s} the number of bonds in the surface layer, V_{s} the volume of the surface cell, and $\boldsymbol{\alpha}^{\mathrm{s}}_i$ is a dressed polarizability within the surface layer. Likewise,

$$\boldsymbol{\chi}_{\mathrm{b}}(\boldsymbol{k}, \omega) = \frac{1}{V_{\mathrm{b}}} \sum_i^{N_{\mathrm{b}}} \boldsymbol{\alpha}^{\mathrm{s}}_i(\boldsymbol{k}, \omega). \tag{22}$$

For a bulk cell of tetrahedral coordination, $N_{\mathrm{b}} = 4$. Within this approach, the normalized change in reflectivity is given by [65]

$$\frac{\Delta R_{\nu}}{R} = \frac{4d\omega}{c} \mathrm{Im}\left(\frac{\epsilon^{\nu\nu}_{\mathrm{s}}(\omega) - \epsilon(\omega)}{\epsilon(\omega) - 1}\right), \tag{23}$$

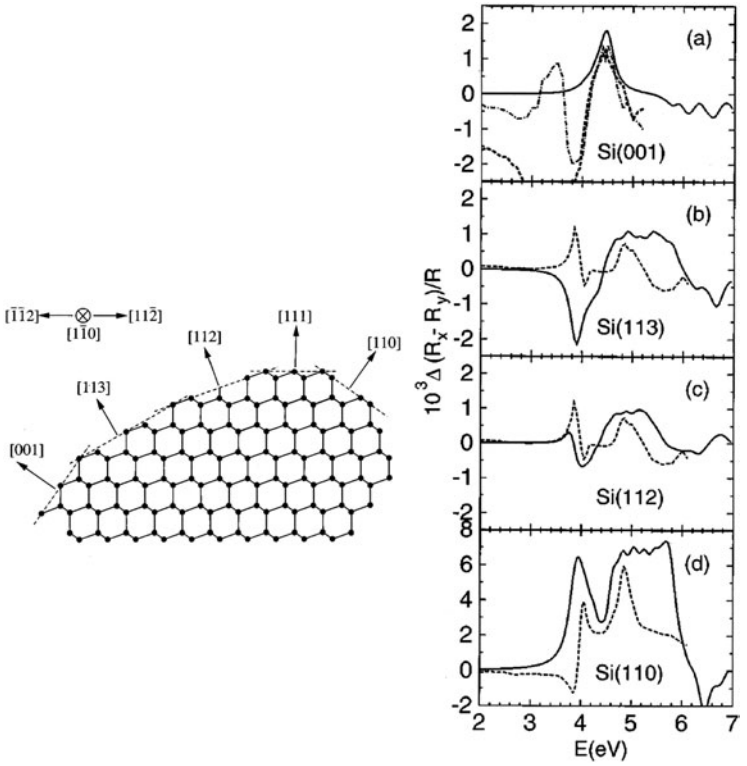

Figure 2. RAS spectra calculated using the discrete dipole model (DDM) (solid curves) and from experiment (dashed curves). Calculated spectra have been scaled by the factors shown in brackets. (a) Si(001) (DDM × $\frac{1}{10}$) and Si(001)-(1 × 2) (dashed curve) and Si(001)-(1 × 2):As (dot–dashed curve), (b) Si(113) (DDM × $\frac{1}{10}$) and Si(113)-H, (c) Si(112) (DDM × $\frac{1}{10}$) and Si(113)-H [76], (d) Si(110) (DDM × $\frac{1}{2}$) and Si(110)-H [76]. Figures taken from [45].

where $\epsilon_s^{\nu\nu}(\omega) = 1 + \chi_s^{\nu\nu}(\boldsymbol{k} = 0, \omega)$, assuming that the normal incident field is polarized along the ν direction, and the isotropic bulk dielectric function is $\epsilon(\omega) = 1 + \chi_b(\boldsymbol{k} = 0, \omega)$. With equations (23) and (7), one can finally obtain the RAS signal for the local models. Equation (23) is equivalent to equation (8).

As an example of this model, we show the RAS spectra calculated for (001), (113), (112), (111) and (110) silicon surfaces in [45]. These surfaces can be generated by cleaving a crystal in a plane containing the [111] direction and a vector perpendicular to that direction, which makes an angle of 54.7°, 29.5°, 19.5°, 0.0° or −35.4° with the [111] direction, respectively. A side view of the surfaces is shown in figure 2. For each surface the x direction is parallel to the [111] direction, and the y direction lies along one of the dotted curves at the surface in figure 2 in a right-handed reference frame.

In figure 2 the spectra for the four surfaces for which experimental data were available [77, 78, 76] are compared to the calculated RAS spectra. The experimental spectra are unscaled in intensity but they have been shifted in energy. The calculated RAS spectra have been scaled by factors given in the figure caption. When discrete dipole spectra are compared to experimental spectra, the magnitude of the RAS intensity for the (112), (113) and (001) surfaces in the discrete dipole spectra is approximately ten times too large and for the (110) surface it is approximately four times too large. Furthermore, peaks in the discrete dipole

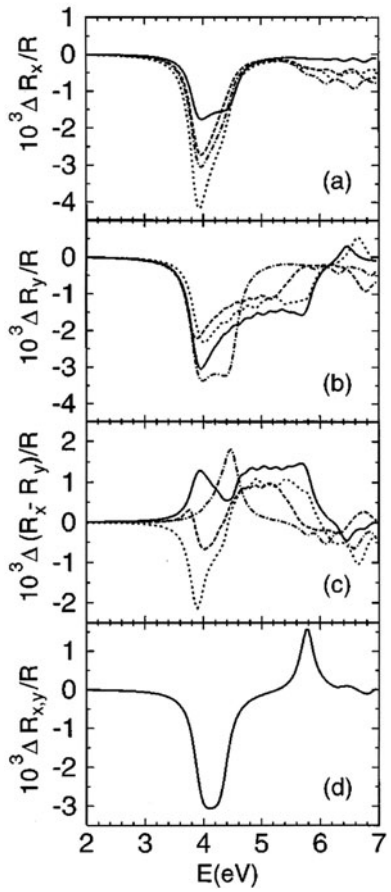

Figure 3. (a) $\Delta R_x/R$, (b) $\Delta R_y/R$, and (c) RAS spectra calculated using the discrete dipole model for surfaces (100) dot–dashed and (110) solid curves. (d) $\Delta R_{x,y}/R$ for the (111) surface. Note $\Delta R_x/R = \Delta R_y/R$ from symmetry considerations. Figure taken from [45].

spectra are shifted upwards in energy with respect to the experimental spectra. There are shifts of 0.6 eV for the (112) and (110) surfaces and there is a shift of 0.3 eV for the (001) surface. The omission of exchange interactions between charge densities induced by the external field in the discrete dipole calculation may be responsible for the energy shift mentioned above [45]. Also, the overestimate of the intensities of the RAS spectra may be due to the fact that real surfaces usually consist of sets of domains that are rotated with respect to each other by 90°, thus inducing a reduction of the RAS intensity. On the other hand, there is an arbitrariness introduced by the damping parameter γ in the intensities of the RAS spectra predicted by the discrete dipole model [45].

Figure 3(a) shows $\Delta R/R$ spectra with the electric field E parallel to the x direction. The (001), (113), (112) and (110) surfaces all have minima in their $\Delta R/R$ spectra at 3.95 eV. $\Delta R/R$ spectra with the electric field parallel to the y direction (figure 3(b)) show minima spread over a small range of energies. The minimum occurs at 3.87 eV for the (112) surface, at 3.95 eV for the (100) and (110) surfaces, and at 4.05 eV for the (113) surface. The (100) and (110) surfaces, therefore, have minima at the same energy for both x and y directions and the (112) and (113) surfaces have minima in $\Delta R/R$ at energies that depend on crystal azimuth. The curves in figure 3(c) are the differences in the curves in figures 3(a) and (b). These are the RAS spectra predicted by the discrete dipole model. One of the surprising features of the calculated RAS spectra is that they change markedly from one surface to another, yet the

quantities used to construct them are quite similar. The $\Delta R/R$ spectrum for the (111) surface is shown separately in figure 3. This surface has no RAS by symmetry and the $\Delta R/R$ spectra for the x and y directions are identical.

The same model has been used for Si(001)1×2-As covered surfaces where same qualitative results have been obtained and where the comparison with experiment is also good [65].

5. Phenomenological models

In this section we discuss the phenomenological models. The dynamics of the induced dipole is given by an equation similar to equation (15), but the site polarizability is replaced by an effective polarizability, $\alpha_{\rm eff}(\omega)$, such that

$$\boldsymbol{P}_i = \alpha_{\rm eff}\left(\boldsymbol{E}_i^{\rm ext} + \sum_j \boldsymbol{T}_{ij}\cdot\boldsymbol{P}_j\right), \tag{24}$$

where $\boldsymbol{P}_i$ is the dipole moment of the ith entity, $\boldsymbol{E}_i^{\rm ext}$ is the external field at the ith entity, and $\boldsymbol{T}_{ij}$ is the dipole–dipole interaction tensor between entity i and j, given by equation (16). In the case of point polarizable atoms occupying the lattice sites of a crystal and interacting between themselves through the dipolar field only, $\alpha_{\rm eff}$ would be the atomic polarizability α. However, this identification may fail for the noble-gas solids, where $\alpha_{\rm eff}$ is modified by the confinement of each atom by nearby atoms and by the multipolar and van der Waals interactions, and for covalent crystals in which there is overlap between the electronic orbitals of nearby atoms, giving rise to an exchange interaction [49]. Also, as discussed in the previous sections, $\alpha_{\rm eff}$ is a function of position since, in general, it depends on the density and the geometrical arrangement of the nearby atoms, and because of the presence of non-dipolar interactions it also depends on the spatial behaviour of the fields, i.e. it is a non-local quantity.

However, $\alpha_{\rm eff}$ may still be interpreted as an effective polarizability, where $n_0\alpha_{\rm eff}$ is the susceptibility that the crystal would have if the dipolar interactions between entities were turned off, with n_0 the density of entities. Thus, taking this interpretation, we can use the Clausius–Mossotti relationship of equation (10), that for a cubic crystals in the long wavelength limit is exact, or its generalized version of equation (9), and use the experimental value of the bulk dielectric function $\epsilon(\omega)$ to obtain $\alpha_{\rm eff}$. In this way, $\alpha_{\rm eff}$ is dressed by the whole self-interaction of each entity, and by exchange, correlation and any other non-dipolar interaction between nearby entities [49]. In principle, $\alpha_{\rm eff}$ depends on the environment of each entity, and thus it is different for the entities near the surface. However in order to investigate the effects of the change in the dipolar contribution to the local field near the surface of cubic crystals, changes in $\alpha_{\rm eff}$ at the surface are usually neglected and thus only bulk values are used.

5.1. Semiconductor surfaces

In [49], the RAS of Ge(110) is calculated, where the only external inputs of the calculation are the experimental $\epsilon(\omega)$ and the lattice structure, and no adjustable parameters. However, one must choose the polarizable entities. Since Ge has a diamond structure, the polarizable entities are tetrahedra, each with a Ge ion at its centre, four shared Ge ions at the vertices (see inset of figure 4) and four doubly occupied electronic orbitals joining the centre to the vertices. These tetrahedra are arranged in an FCC lattice with the lattice constant of Ge. Such a choice minimizes the non-dipolar interactions between nearby entities [49].

The calculated RAS spectrum is shown in figure 4 together with experimental results of [79]. The calculation predicts a reasonable line shape and is of the correct order of magnitude.

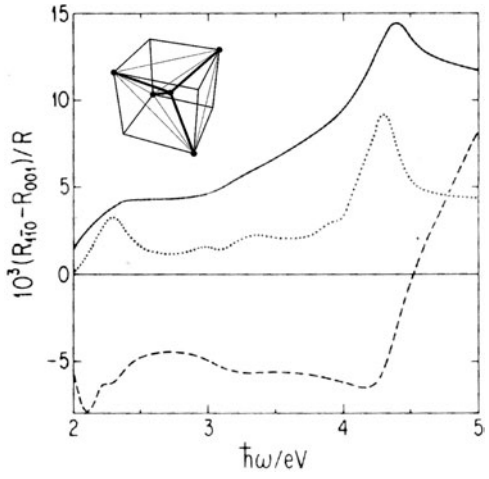

Figure 4. Normal-incidence RAS spectra of a Ge(110) surface versus frequency: FCC calculation (solid curve), diamond-lattice calculation (dashed curve) and experimental result (dotted curve). Plot figure taken from [49]. Inset: tetrahedral polarizable entity, whose FCC lattice built the diamond structure.

As could be expected, they overestimated the surface local field effect since every two finite-sized Ge atoms are replaced by one point polarizable entity. In the same figure, a calculation of the RAS spectrum choosing single Ge atoms occupying a diamond lattice as polarizable entities is shown. The striking discrepancy with experiment shows that this is not a fortunate choice. The reason for this is that the interaction between neighbouring Ge atoms is dominated by the covalently shared electrons, which is mostly non-dipolar.

To circumvent the choice of the polarizable entity, in [46], point dipoles are located at the centre of the interatomic bonds forming a polarizable bond model. Then, the crystal is composed of an array of individual point-like dipoles (bonds). Every dipole is considered to be an anisotropic point-like harmonic oscillator of cylindrical symmetry whose $\alpha_{\rm eff}$ is given by equation (17), with $\perp = \perp'$, and the index i expanding the four bonds λ (with different orientation) and the plane number n (surface or bulk) of a given tetrahedra. Therefore, the microscopic polarizability of each dipole, indeed, depends on its position through its particular bond orientation and its surface or bulk location. In this model we use the generalized Clausius–Mossotti (CM) relationship implied by equation (9) to relate $\epsilon(\omega)$ to $\alpha_\perp(\omega)$ and $\alpha_\parallel(\omega)$. Close to the visible, we expect that the main contribution to $\alpha_\parallel$ originates in bonding–antibonding transitions, while $\alpha_\perp$ is due to transitions involving atomic states. Thus, we approximate

$$\alpha_\perp(\omega) = \frac{(f\omega_{\rm p})^2}{\omega_\perp^2 - \omega^2 - {\rm i}\omega_c\omega}, \tag{25}$$

where once $\omega_{\rm p}$, $\omega_\perp$ and ω_c (adjustable parameters) are chosen, the CM relation is solved for each frequency to obtain $\alpha_\parallel(\omega)$ in terms of the experimentally measured bulk dielectric function $\epsilon(\omega)$. Here, the factor $f = 1$, but it will be used in the next example.

Once we have $\boldsymbol{\alpha}^\lambda(\omega)$, from equation (24) we can write [46],

$$\boldsymbol{P}_{n\lambda}(\omega) = \boldsymbol{\alpha}^\lambda(\omega) \cdot \left(\boldsymbol{E}^{\rm ext}(\omega) + \sum_{n',\lambda'} \boldsymbol{M}_{n\lambda,n'\lambda'} \cdot \boldsymbol{P}_{n'\lambda'}(\omega) \right), \tag{26}$$

where the term in parenthesis is the local field, which is the sum of the external field $\boldsymbol{E}^{\rm (ext)}(\omega)$ (assumed to be constant) and the dipolar field produced by all other bonds. A *plane wise summation* [67] over equivalent bonds that belong to the same plane has been done, and thus from equation (16) one can derive $\boldsymbol{M}_{n\lambda,n'\lambda'}$, which is the dipole–dipole interaction tensor between the λ-dipole in plane n and the λ'-dipole in plane n', where self-interaction is excluded from the summation in equation (26) [46].

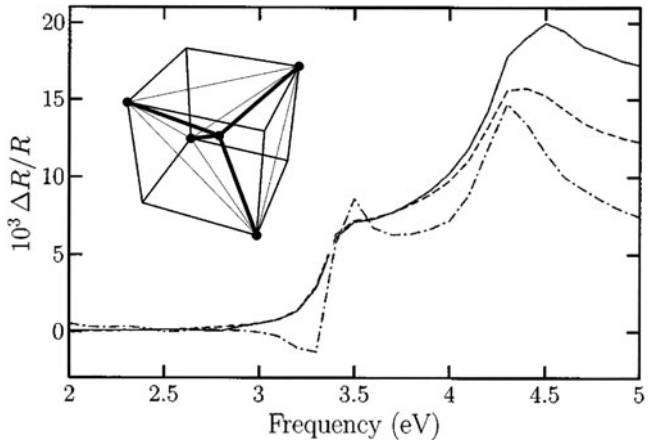

Figure 5. Normal incidence anisotropy of the linear reflectance $\Delta R/R$ of a Si(110) surface as a function of frequency ω. We show results calculated with the bond model (solid curve) and for a single FCC lattice of isotropic tetrahedral polarizable entities (dashed curve) together with experimental results (dashed–dotted curve). Figure taken from [46]. We mention that $\Delta R/R \equiv$ RAS. Inset: illustration shows a tetrahedral building block consisting of a cube with Si atoms at alternate vertices joined to another Si atom at the cube's centre by four bonds. Each bond is replaced by a point polarizable dipole.

Following this procedure, in [46] the RAS signal for a Si(110) ideally terminated surface was calculated where the normally incident light is polarized along the [110] and [001] directions. The results are shown in figure 5 along with experimental data [79] and also the results for a simple FCC lattice of dipoles [29]. We notice that the bond model has good agreement with the experiment, as good as that of the single-FCC model. For the calculated spectra, the surface was taken to be ideally terminated, and no relaxation or reconstruction was taken into account. Nevertheless the qualitative results are rather good and the main physics seems to be captured through the local field. It is worth mentioning that fully microscopic models for this surface have been proposed [29, 13], and just recently an adequate but numerically intricate model [16] has been able to give similar results as the ones obtained through the polarizable bond model.

In [43] the model described above is used to calculate the RAS spectra of Si(100) for fully relaxed 2×1 and 4×2 surfaces that are characterized by the presence of a buckled surface dimer (see figure 6). To account for the charge transfer between the dimer atoms that is concomitant with the buckling, one has to allow for the factor f of equation (25) to be $\geqslant 1$ for the dipole representing the dimer, and $f = 1$ for all other dipoles, taking ω_{p} as a fixed value. Also, for the bond corresponding to the dimer, the actual position of the dipole may be off centred due to this charge transfer to the upper atom that takes place as the surface reconstructs. Figure 6 shows RAS spectra of the Si(100)2×1 surface for three surface reconstructions with different buckling, along with the experimental results of [80, 81] performed on highly oriented single-domain surfaces. All dipoles, including the dimers, have identical $\alpha(\omega)$, with $f = 1$. All theoretical spectra show three features above 3.5 eV that are near the experimentally determined values of 3.6, 4.3 and 5.3 eV. However, only the surface with a buckling of 0.7 Å gives the RAS spectrum features having correct signs at 3.9 and 4.2 eV, in qualitative agreement with experiment. The RAS spectrum for the surface with symmetric dimers shows a feature at 3.3 eV in correspondence with the experimental one at the same energy. However this case also shows a broad and large negative structure at 2.4 eV not seen

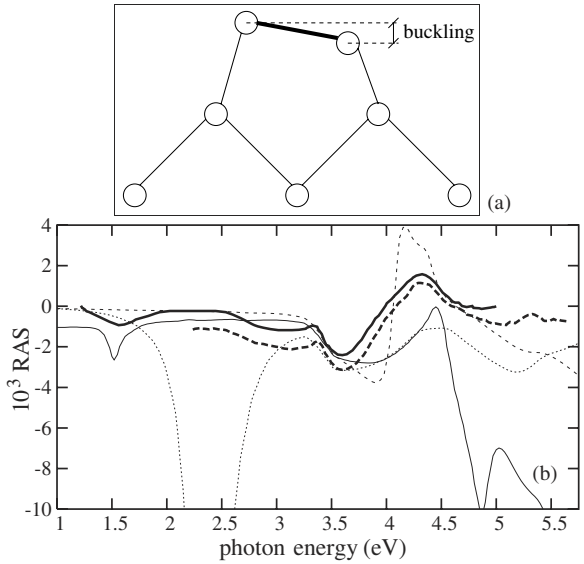

Figure 6. (a) Si(100)2 × 1 reconstructed surface showing the dimer buckling. (b) RAS spectra of the clean Si(100)2 × 1 surface for different dimer bucklings: 0 Å (symmetric dimers) (dotted curve), 0.6 Å (thin-solid curve) and 0.7 Å (dashed curve). The experimental spectra are also shown: for RAS the thick-solid curve is from [80] and the thick-dashed curve is from [81]. Figure taken from [43].

in the experimental curves. In addition, only the RAS spectrum of the geometry with buckling of 0.6 Å has a feature at 1.5 eV, which qualitatively reproduces the experimental one at 1.6 eV. Similar results at 1.5 and 4.3 eV are reported in [14], but the RAS spectra calculated there have several features between 1.5 and 4.0 eV that are not present in the experimental data and in the spectra of figure 6.

In a tilted dimer there is a charge transfer of $\sim e/3$ into the upper Si atom of each buckled dimer [82]. In order to include such a charge transfer in the model, the following two variables can be adjusted: (a) f for the dimer alone, since it is proportional to the dimer electronic density, and (b) the position of the point dipole that replaces the dimer's bond, from its nominal centred position $\Delta = 0$ to an off-centred position $\Delta \neq 0$, since the charge is redistributed in the same manner as its centroid (see figure 7 (a)). In [43], it is found that for the surface with a buckling of 0.6 Å, the best RAS spectrum is given for $f = 1.9$ and $\Delta = 0.25a$ towards the upper Si atom of the dimer where a is the dimer's bond length, and the results are shown in figure 7. Comparing the spectra, we see that the spectrum for $\Delta = 0.25a$ gives a much better line shape than that of $\Delta = 0$ (whose spectrum is larger by a factor of 2), since the RAS feature at 1.5 eV is very well defined. Also the RAS spectrum qualitatively reproduces the small feature seen in the experiment of [81] above 5 eV. On the other hand, if we use a negative Δ, which would imply an off-centred dipole towards the lower Si atom in the dimer, we obtain RAS spectra which do not agree with experiment, thus confirming the prediction of [82] through this optical model.

5.2. Organic thin films

Recently, in [58], the polarizable bond model has been applied to study the RAS optical properties of organic thin films, in particular porphyrin layers deposited onto gold substrates by the Langmuir–Schaefer technique. This is because molecular materials have aroused interest in recent years due to their potentiality in nanotechnology where the characterization of electronic states is essential. RAS has been applied to organic layers, showing that anisotropies are related to electronic properties of the molecule and to the morphological characteristics of the layer [58, 84–86]. The optical activity of the porphyrin molecule is represented by a polarizable dipole that responds to the incident light like a harmonic oscillator. Using

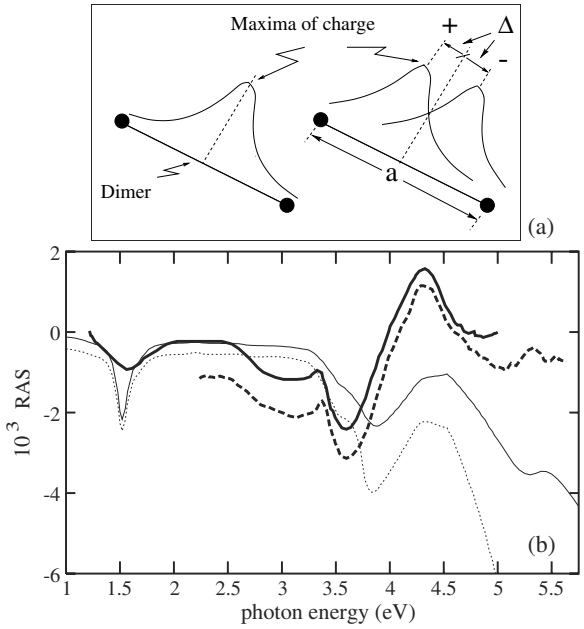

Figure 7. (a) Dimers of the clean Si(100)2 × 1 surface. The curves show the distribution of charge. Figure taken from [83]. (b) RAS spectra of the clean Si(100)2 × 1 surface with dimer buckling of 0.6 Å. The dotted curve is for $\Delta = 0$, whereas the thin-solid curve is for $\Delta = 0.25a$, which gives the dimer's dipole displaced towards the upper Si by 0.25 of its length. Both spectra have the same $f = 1.9$. Figure taken from [43].

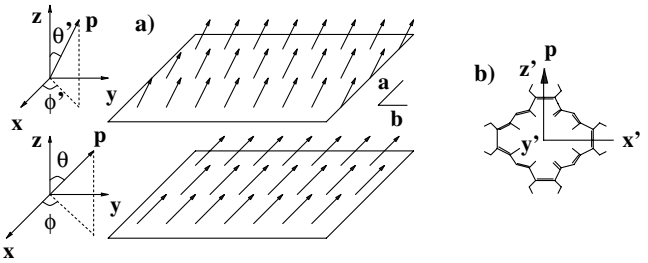

Figure 8. (a) The arrows represent the polarizable entities with a tilt angle θ and a twist angle ϕ. The planes with arrows represent a stack of several layers, with equal θ and ϕ, thus the upper plane shows a change in tilt and twist with respect to the lower plane. x, y, and z are the system's coordinates. (b) Structure of the porphyrin and its total polarizable dipole moment along the principal axis, z', of the porphyrin. Figure taken from [58].

the porphyrin's coordinate system, we assume that α is diagonal and has only one resonant frequency, implying that the molecule only polarizes along its principal axis (see figure 8). Thus we can write

$$\alpha_{\parallel}(\omega) = \frac{\alpha_0}{\left[1 - (\omega/\omega_0)^2 - \mathrm{i}(\omega/\omega_0)(1/(\omega_0\tau))\right]}, \tag{27}$$

where ω_0 is the unique resonant frequency, τ is a damping parameter related to the width of the resonance, and α_0 is the value of the static dipole moment of the porphyrin.

The layers of porphyrins are reproduced by a model system consisting of N identical non-overlapping polarizable entities regularly distributed in a plane with the same dipole orientation characterized by angles θ and ϕ with respect to the plane's coordinate system (see figure 8). The polarizable entities, or layers, characterized with a dielectric function $\epsilon_1(\omega)$, sit on top of an isotropic substrate, also characterized by a dielectric function $\epsilon_2(\omega)$. The Langmuir–Schaefer technique ensures a highly ordered deposition of the porphyrin molecules, which we assume are sitting in a rectangular lattice, with lattice parameter a and b along the two mutually

perpendicular x and y directions along the plane, and even interlayer spacing d perpendicular to the substrate, i.e. along z. For simplicity we assume that the first layer sits a distance d on top of the substrate. Since all the dipoles in a given layer, ℓ, are identical, the induced dipole moment, $p_i(\ell, \omega)$, would be identical too, and is given through equation (24), which we write explicitly for convenience

$$p_i(\ell,\omega) = \alpha_{ij}(\ell,\omega)\Bigg[E_j + \sum_{\ell'}\Bigg(T_{jk}(a,b)\delta_{kl}\delta_{\ell\ell'} + \mathcal{T}_{jk}(a,b,|d_\ell - d_{\ell'}|)\delta_{kl}(1-\delta_{\ell\ell'}) + \frac{\epsilon_2-\epsilon_1}{\epsilon_2+\epsilon_1}\mathcal{T}_{jk}(a,b,|d_\ell + d_{\ell'}|)S_{kl}\Bigg)\Bigg]p_l(\ell',\omega), \tag{28}$$

where ℓ, ℓ' go from one up to the total number of layers, L. Summing over repeated $i, j, k, \ldots$ Cartesian indexes is assumed. The term $T_{ij}(a, b)$ is recognized as the dipolar interaction tensor that gives the local field contribution of the entities on the same plane, and $\mathcal{T}_{ij}(a, b, z)$ as that of the entities in plane ℓ with those of plane ℓ', with z the inter-plane separation and d_ℓ the vertical position of the ℓth plane. However the third term gives the contribution of the planes on top of the substrate, whereas the fourth term gives the contribution coming from the images located inside the substrate, as can be recognized by the screening factor given by the dielectric functions, and $S_{ij} = \mathrm{diag}(-1, -1, 1)$ to give the correct orientation of the image dipoles. Both $\boldsymbol{T}$ and $\boldsymbol{\mathcal{T}}$ have been summed over all the entities in the corresponding planes using the plane-wise summation technique of [67]. To solve equation (28), we need to go from $\alpha_\parallel(\omega)$ of equation (27) into $\alpha_{ij}(\ell, \omega)$, which is done by a simple transformation from the porphyrin axis to the coordinate system of the sample [58]. From equation (8) the RAS signal of the system, $\mathcal{R}$, is given by

$$\mathcal{R} \equiv 4\pi\left(\frac{d}{\lambda}\right)\frac{1}{p_0}\,\mathrm{Im}\sum_{\ell=1}^{L}\left[p_x(\ell,\omega) - p_y(\ell,\omega)\right], \tag{29}$$

with λ the wavelength of the incident light and p_0 a normalization factor with the units of dipole moment and proportional to α_0, which is used to set the scale of $\mathcal{R}$.

For simplicity $a = b = d$, i.e. a cubic lattice, $d_\ell = \ell d$, $\epsilon_1(\omega) = 1$ and $\epsilon_2(\omega)$ given by the experimental values for gold [87]. Then, besides the number of layers L, θ and ϕ are the only variables in the model. Since $a = b$ one would expect $\mathcal{R} = 0$ since the system is isotropic, but if we allow for the porphyrins to be tilted and twisted with respect to the substrate, i.e. $\theta \neq 0$ and $\phi \neq 0$, the RAS signal would be different from zero. Since the substrate is isotropic the x and y axes are chosen arbitrarily. To choose ω_0 and τ we use the experimental results of the UV–visible absorption spectrum of [84], where a dominant Soret band is seen at $\omega_0 = 387\ \mathrm{nm}^{-1}$, with $\omega_0\tau = 0.25$.

Here we only are going to show the main results; details of the model can be found in [58]. In figure 9 we show $\mathcal{R}$ changing L from 2 up to 16 in steps of 2, and for each corresponding change in L we decrease θ by 2° and increase ϕ by 1.2°, starting at $\theta = 58°$ and $\phi = 30°$ for $L = 2$. Indeed, as L is increased $\mathcal{R}$ goes from peak-like to derivative-like, just as in the experiment (also shown), indicating that the model qualitatively reproduces in terms of the geometrical reordering of the porphyrin layers the experimental trend as L is increased [84]. In the same figure, we show $\mathcal{R}$ when ϕ is fixed to 30°, where we see that the agreement in the short wavelength region is not as good, and therefore the azimuthal variation that we introduced also induces a twist in the porphyrins that is required in order to get agreement with the experiment. The same behaviour is found when the substrate changes from a metal to a dielectric, thus changing $\epsilon_2(\omega)$ which controls the image term in equation (28). Since the interlayer local field interaction decays exponentially with z, the image's contribution is only marginal. Thus, the model would apply to the films of [85] grown by the Langmuir–Blodgett technique on a quartz substrate.

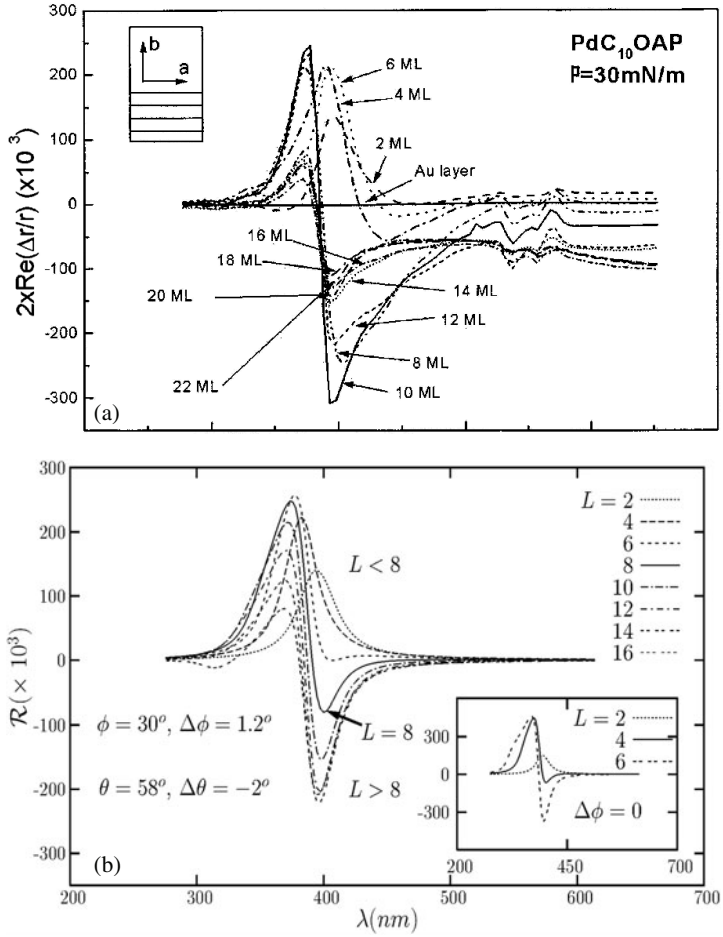

Figure 9. (a) Experimental results taken from [84]. (b) $\mathcal{R}$ versus λ for different values of L, θ and ϕ. In the main panel, θ decreases by 2° and ϕ increases by 1.2°. In the inset $\phi = 30°$ is fixed and θ varied as in the main panel. Figure taken from [58].

The decrease of θ as the number of layers is increased could be understood by the fact that the interaction with the substrate will be screened by the underlying layers, thus producing porphyrins which will try to align along the substrate normal. This is in agreement with the reasoning of [84] that attributes the interaction with the substrate to π orbitals of the porphyrin. However, the twisting comes out of the model, and the increment of ϕ is needed from the fact that the correct magnitude of p_x and p_y is required to reproduce the experimental derivative-like feature in $\mathcal{R}$. Then, as ϕ is increased p_y grows while p_x decreases simply from the geometrical projection along the two perpendicular axes where one measures the RAS signal. The behaviour of the system is ultimately driven by the local field among the porphyrins.

5.3. Metal surfaces

The polarizable bond model has also been applied to metals. Recently, a RAS signal of the order of 10% was measured in a Ag(110) single crystal surface [88]. This value is rather large, especially in view of the fact that the typical RAS signal is smaller than 0.1%. In a metal one has to account not only for the bounded electrons, like in the semiconductors or organic

molecules of the previous sections, but also for the free electrons which tend to dominate the dynamics. Therefore, one has to consider both d (bounded) and s–p (free) electrons into the model. First, one considers that the d electrons are mostly localized around the ionic core positions, whereas the s–p conduction electrons are delocalized. Indeed, in [89], one then assumes that the d electrons are confined within an imaginary sphere centred around each ion, while the interstitial region outside the spheres contains predominantly conduction electrons. The Ag crystal is then modelled by a uniform electron gas where spherical cavities centred at FCC lattice sites are craved. The polarization of each cavity is described by a point dipole, $\boldsymbol{p}_i$ located at its centre (i), whose polarizability $\alpha(\omega)$ accounts for inter band transitions, the conduction current within the spheres, core polarization and all intra-cavity interactions. In [89], it is further argued that these induced dynamical dipoles are the sources of an electric field which is screened by the surrounding electron gas, located in the interstitial region, and characterized by a local Drude dielectric function $\epsilon_{\mathrm{g}}(\omega) = 1 - \omega_{\mathrm{p}}^2/(\omega^2 + \mathrm{i}\omega\tau^{-1})$, where ω_{p} is the free-electron plasma frequency and τ the relaxation time. The calculations shown that the choice of ω_{p} and τ of the interstitial free-electron gas has little influence on the RAS spectra [88]. Now, as follows from equation (24),

$$\boldsymbol{p}_i = \alpha(\omega)\boldsymbol{E}_i^{\mathrm{loc}}, \tag{30}$$

where the local electric field $\boldsymbol{E}_i^{\mathrm{loc}}$ at site i is the sum of the external field screened by the semi-infinite electron gas, the fields created by all the other dipoles, $\boldsymbol{p}_j$, and the fields created by the images of all the dipoles through the surface of the electron gas. The polarizability $\alpha(\omega)$ of the dipoles is determined by the Clausius–Mossotti relationship (10), now written to take the background of the free electrons into account as

$$\frac{\epsilon(\omega) - \epsilon_{\mathrm{g}}(\omega)}{\epsilon(\omega) + 2\epsilon_{\mathrm{g}}(\omega)} = \frac{4\pi n\alpha}{3}, \tag{31}$$

where $\epsilon(\omega)$ is the Ag bulk dielectric function and n is the number density of ions. Standard spectroscopic ellipsometry experiments were performed in order to determine $\epsilon(\omega)$ of the samples. After equation (30) is solved numerically by the *plane wise* technique [67, 89], the RAS signal could be obtained from equation (7). However, figure 10 shows both the real and the imaginary part of $\Delta r/r = (r_{[1\bar{1}0]} - r_{[001]})/r_{[001]}$, where $r_{[1\bar{1}0]}$ and $r_{[001]}$ are the complex reflectances for the electric field aligned along the $[1\bar{1}0]$ and the [001] directions, respectively [88]. The RAS signal and $\Delta r/r$ are closely related.

In figure 10 the experimental results for a Ag(110) clean and slightly contaminated surface are shown, along with the theoretical results. The agreement with the experimental data is very good, indicating that the model provides a good description of an Ag crystal. The magnitude of the anisotropy increases with the surface contamination. This can be attributed to the growth of a sulphur overlayer which reduces r, hence the denominator in $\Delta r/r$. The model assumes an abrupt interface and very localized d electrons, so it most probably overestimates the surface local field effect and therefore agrees better with experiments on the most contaminated sample. The origin of the observed RAS is the very large deviations of the reflectances of the Ag(110) surface for both symmetry directions from the Fresnel reflectance. These deviations are due to large resonant surface optical absorptions corresponding to self-sustained dipolar oscillations localized close to the surface [89]. The surprisingly large size of the RAS has two different origins. On the one hand, the surface local field effect shifts the resonance to the plasma frequency region (3.78 eV) where dissipation is small, so that the induced dipoles display values about one order of magnitude larger than in others systems. The electrostatic interactions between the corresponding dipoles, screened by the Ag free electrons, depend on the direction of the applied electric field with respect to the surface, leading to different shifts

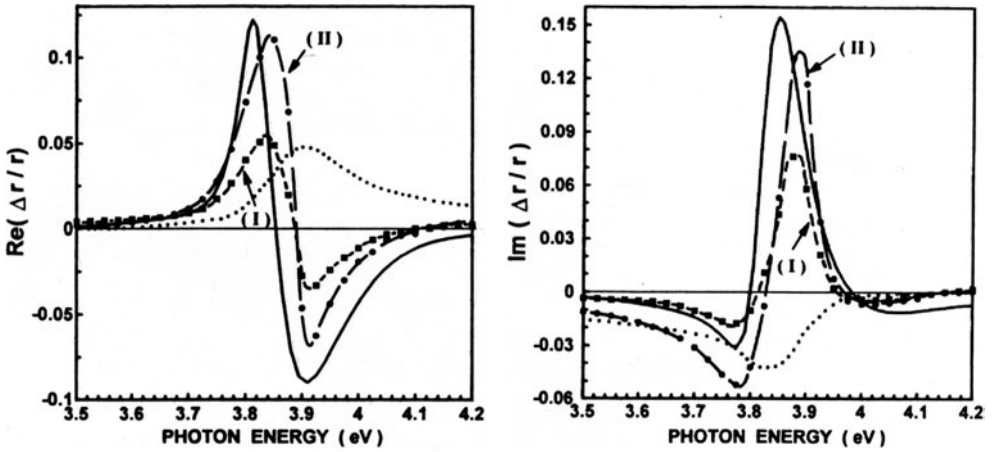

Figure 10. (a) Real part of the reflectance anisotropy. Short-dashed curve (I): experimental data for the clean sample; long dashed curve (II): experimental data for the contaminated sample. Dotted curve: simple calculation based on the phenomenological result of [90]. Solid curve: local field effect calculation. (b) Imaginary part of the reflectance anisotropy. Same as (a). Figures taken from [88].

in the resonance for the [001] and [1$\bar{1}$0] directions. On the other hand, the small values of the reflectance r around 3.9 eV, enhance the size of $\Delta r/r$ by another order of magnitude.

6. Conclusions

We have reviewed the polarizable dipole models used in the literature in order to calculate the reflectance anisotropy spectroscopy, and presented some of the most successful examples for different surfaces that range from semiconductors to organic films and metals. These models visualize an ordered array of polarizable units or dipoles that replaces the crystalline structure of the system in question. They treat a valence electron pair (bond) or the suitable basic cell as a point-like polarizable unit which responds to the local field by creating a dipole moment there. The interaction among the dipoles is driven by the local field, and depending on the approach followed, three different levels of sophistication were presented for the calculation of this local field and the basic dynamical response of the dipole, through its microscopic polarizability.

The utility of these models stems from the fact that they offer, with minimal computational effort, answers to questions that are not easily obtained from a band structure calculation. We can expect to answer questions such as: how far from a semiconductor surface is the bulk of the solid? Or, when an electromagnetic field is incident on a surface, how much does the local field do? Or, how is a Coulombic field screened by dipoles in a semiconductor? Although we did not dwell on these questions, they are answered in the cited literature. Also, the adjustable parameters are kept to a minimum, and it is the geometry of the surface, through the local field, that induces the optical anisotropies.

There are other contributions to the surface induced anisotropy. Some are extrinsic such as directional surface roughness, and others are intrinsic such as transitions involving surface states and surface modified bulk states. Their relative importance depends on the surface preparation. However, the close agreement between these essentially parameter-free models and the experiments demonstrate the importance of the surface local field effect at semiconductor, organic and noble metal surfaces.

In conclusion, the polarizable dipole models are very useful in understanding some of the physics involved in the RAS response of a surface, and the information they provide should be used along with the quantum mechanical models based on band structure calculations and the experimental results in order to have a complete story of this very fascinating optical phenomena.

Acknowledgments

We are grateful for partial support from CONACyT-México (BSM grant 36033-E) and CONCYTEG-México (BSM grant 03-04-k119-049; RV grant 03-04-k118-039 anexo 5 and 04-04-K117-011 anexo 4; N A 03-04-K118-039, anexo 3 and 04-04-K117-011 anexo 2).

References

[1] For a review see the articles in Mendoza B S (Guest ed) 2003 *Phys. Status Solidi* c **0** Optics of surfaces and interfaces (OSI-2003)
[2] Esser N and Richter W (Guest ed) 2001 *Phys. Status Solidi* a **188** (4) 2001 WE-Heraeus-Seminar Optical Spectroscopy at interfaces (OSI-2001)
[3] Downer M C, Mendoza B S and Gavrilenko V I 2001 *Surf. Interface Anal.* **31** 966
[4] Lüpke G 1999 *Surf. Sci. Rep.* **35** 75
[5] Weightman P 2001 *Phys. Status Solidi* a **188** 1443
[6] Richter W 1993 *Phil. Trans. R. Soc.* A **344** 453
[7] Aspnes D E, Colas E, Studna A A, Bhat R, Koza M A and Keramidas V G 1988 *Phys. Rev. Lett.* **61** 2782
[8] Harrison P, Farrell T, Maunder A, Smith C I and Weightman P 2001 *Meas. Sci. Technol.* **12** 1
[9] Richter W and Zettler T 1996 *Appl. Surf. Sci.* **100/101** 465
[10] Mochán W L and Barrera R G 1984 *J. Physique Coll.* **45** C5 207
[11] Mendoza B S, Esser N and Richter W 2003 *Phys. Rev.* B **67** 165319
[12] Castillo C, Mendoza B S, Schmidt W G, Hahn P H and Bechstedt F 2003 *Phys. Rev.* B **68** 041310(R)
[13] Mendoza B S, Del Sole R and Shkrebtii A 1998 *Phys. Rev.* B **57** R12709
[14] Palummo M, Onida G, Del Sole R and Mendoza B S 1999 *Phys. Rev.* B **60** 2522
[15] Pulci O, Onida G, Del Sole R and Reining L 1998 *Phys. Rev. Lett.* **81** 5374
[16] Hahn P, Schmidt G and Bechstedt F 2002 *Phys. Rev. Lett.* **88** 016402
[17] Rohlfing M and Louie S G 1999 *Phys. Rev. Lett.* **83** 856
[18] Born M and Huang K 1954 *Dynamical Theory of Crystal Lattices* (London: Oxford University Press) pp 248–55
Born M and Huang K 1954 *Dynamical Theory of Crystal Lattices* (London: Oxford University Press) pp 398–401
[19] Jackson J D 1975 *Classical Electrodymanics* 2nd edn (New York: Wiley) section 4.5
[20] Maradudin A A, Montroll E W, Weiss G H and Ipatova I P 1971 *Theory of Lattice Dynamics in the Harmonic Approximation* (New York: Academic)
[21] Vlieger J 1973 *Physica (Amsterdam)* **64** 63
[22] Phipott M R 1973 *Adv. Chem. Phys.* **23** 227
[23] Phipott M R and Lee J W 1973 *J. Chem. Phys.* **58** 595
[24] Lehnen A P and Bruch L W 1980 *Physica* A **100** 215
[25] Lekner J and Castle P J 1980 *Physica* A **101** 89
[26] Bagchi A, Barrera R G and Fuchs R 1982 *Phys. Rev.* B **25** 7086
[27] Munn R W 1988 *Mol. Phys.* **64** 1
[28] Chen W and Schaich W L 1989 *Surf. Sci.* **218** 580
[29] Del Sole R, Mochán W L and Barrera R G 1991 *Phys. Rev.* B **43** 2136
[30] Patterson C H, Weaire D and McGilp J F 1992 *J. Phys.: Condens. Matter* **4** 4017
[31] Munn R W 1992 *J. Chem. Phys.* **97** 4532
[32] Wijers C M J, Rasing T and Hollering R W J 1993 *Solid State Commun.* **85** 233
[33] Ewald P P 1916 *Ann. Phys., Lpz.* **49** 117
Ewald P P 1970 *On the Foundations of Crystal Optics* (Cambridge: Airforce Cambridge Research Laboratories) (translations, No. 4 AFCRL-70-0580)
[34] Ewald P P 1917 Dispersion und Doppelbrechung von Elektronengittern *PhD Thesis* Dietrichsschen Universitäts-Buchdruckerei Göttingen p 519
[35] Litzman O and Rózsa P 1977 *Surf. Sci.* **66** 542
[36] Litzman O 1978 *Opt. Acta* **25** 509
[37] Litzman O 1980 *Opt. Acta* **27** 231

[38] Litzman O 1982 *Opt. Acta* **29** 71317
[39] Litzman O, Mikulik P and Dub P 1996 *J. Phys.: Condens. Matter* **8** 4709
[40] Poppe G P M, Wijers C M J and Van Silfhout A 1991 *Phys. Rev.* B **44** 7917
[41] Wijers C M J and Poppe G P M 1992 *Phys. Rev.* B **46** 7605
[42] Wijers C M J, Del Sole R and Manghi F 1991 *Phys. Rev.* B **44** 1825
[43] Arzate N and Mendoza B S 2001 *Phys. Rev.* B **63** 113303
[44] Arzate N and Mendoza B S 2001 *Epioptics 2000: Proc. 19th Course of the International School of Solid State Physics Erice (Sicily, Italy)* (Singapore: World Scientific)
[45] Hogan C D and Patterson C H 1998 *Phys. Rev.* B **57** 14843
[46] Mendoza B S and Mochán W L 1997 *Phys. Rev.* B **55** 2489
[47] Poppe G P M and Wijers C M J 1990 *Physica* B **167** 221
[48] Mochán W L and Barrera R G 1986 *Phys. Rev. Lett.* **56** 2221
[49] Mochán W L and Barrera R G 1985 *Phys. Rev. Lett.* **55** 1192
[50] Aspnes D E, Hansen J-K, Peng H-J, Powell G D and Wang J-F T 2003 *Phys. Status Solidi* b **240** 509
[51] McGilp J F and Carroll L 2003 *Phys. Status Solidi* c **0** 3060
[52] Powell G D, Wang J F and Aspnes D E 2002 *Phys. Rev.* B **65** 205320
[53] Mejía J E and Mendoza B S 2001 *Phys. Status Solidi* a **188** 1393
[54] Cruz-Mandujano J and Mendoza B S 2000 *Phys. Rev.* B **62** 8438
[55] Mendoza B S and Mochán W L 1996 *Phys. Rev.* B **53** R10473
[56] De Boeij P L 1992 *MSc Thesis* Twente University, Enschede, The Netherlands
[57] Schaich W L and Mendoza B S 1992 *Phys. Rev.* B **45** 14279
[58] Castillo C, Vázquez-Nava R A and Mendoza B S 2003 *Phys. Status Solidi* c **0** 2971
[59] Ye P and Shen Y R 1983 *Phys. Rev.* B **28** 4288
[60] Wijers C M J, Boeij P L, Van Hasselt C W and Rasing T H 1995 *Solid State Commun.* **93** 17
[61] McGilp J F, Tang Z-R and Cavanagh M 1993 *Synth. Met.* **61** 181
[62] Hayden L M 1988 *Phys. Rev.* B **38** 3718
[63] Ortiz P G and Mochán W L 2003 *Phys. Rev.* B **67** 184204
[64] Boeij P L and Wijers C M J 2000 *Phys. Lett.* A **272** 264
[65] Patterson C H and Herrendörfer D 1997 *J. Vac. Sci. Technol.* A **15** 3036
[66] Herrendörfer D and Patterson C H 1997 *Surf. Sci.* **375** 210
[67] De Wette F W and Schacher G E 1965 *Phys. Rev.* **137** A78
[68] McIntyre J D E and Aspnes D E 1971 *Surf. Sci.* **24** 417
[69] Alder S L 1962 *Phys. Rev.* **126** 413
[70] Wiser N 1963 *Phys. Rev.* **129** 62
[71] Bechstedt F 2003 *Principles of Surface Physics* 1st edn (Berlin: Springer) p 241
[72] Schmidt W G, Glutsch S, Hahn P H and Bechstedt F 2003 *Phys. Rev.* B **67** 085307
[73] Wijers C M J 2001 *Phys. Status Solidi* a **188** 1251
[74] Wijers C M J and De Boeij P L 2001 *Physica* B **305** 220
[75] Esser N, Hunger R, Rumberg J, Ritcher W, Del Sole R and Shkrebtii A 1994 *Surf. Sci.* **307–309** 1045
[76] Yasuda T, Aspnes D E, Lee D R, Bjorkman C H and Lucovsky G 1994 *J. Vac. Sci. Technol.* A **12** 1152
[77] Kipp L, Biegelsen D K, Northrup J E, Swartz L E and Bringans R D 1996 *Phys. Rev. Lett.* **76** 2810
[78] Yasuda T, Mantese L, Rossow U and Aspnes D E 1995 *Phys. Rev. Lett.* **74** 3431
[79] Aspnes D E and Studna A A 1985 *Phys. Rev. Lett.* **54** 1956
[80] Shioda R and Van der Weide J 1998 *Phys. Rev.* B **57** R6823
[81] Jaloviar S G, Lin J-L, Feng L, Zielasek V, McCaughan L and Lagally M G 1999 *Phys. Rev.* B **82** 791
[82] Chadi D J 1979 *Phys. Rev. Lett.* **43** 43
[83] Arzate N 2000 Second harmonic generation at crystalline semiconductor surfaces *PhD Thesis* Center of Optical Research, México, p 39
[84] Goletti C, Paolesse R, Dalcanale E, Berzina T, Di Natale C, Bussetti G L, Chiaradia P, Froiio A, Cristofolini L, Costa M and D'Amico A 2002 *Langmuir* **18** 6881
[85] Goletti C, Paolesse R, Di Natale C, Bussetti G L, Chiaradia P, Froiio A, Valli L and D'Amico A 2001 *Surf. Sci.* **501** 31
[86] Frederick B G, Power J R, Cole R J, Perry C C, Chen Q, Haq S, Bertrams Th, Richardson N V and Weightman P 1998 *Phys. Rev. Lett.* **80** 4470
[87] Weaver J H, Krafka C, Lynch D W and Koch E E 1981 *Physics Data Series* (Karlsruhe: Fachsinformationzentrum-Energy, Physik, Mathematik)
[88] Borensztein Y, Mochán W L, Tarriba J, Barrera R G and Tadjeddine A 1993 *Phys. Rev. Lett.* **71** 2334
[89] Tarriba J and Mochán W L 1992 *Phys. Rev.* B **46** 12902
[90] Tadjeddine A, Kolb D M and Kötz R 1980 *Surf. Sci.* **101** 277